Steel and Composite Structures, *Vol. 33, No. 2* (*2019*) *209-224*
DOI: https://doi.org/10.12989/scs.2019.33.2.209

An analytical solution to the mapping relationship between bridge structures vertical deformation and rail deformation of high-speed railway

Yulin Feng [1a], Lizhong Jiang [1,2b], Wangbao Zhou*[1,2], Zhipeng Lai [1,3c] and Xilin Chai [1d]

[1] *School of Civil Engineering*, *Central South University*, *Changsha*, *410075*, *China*
[2] *National Engineering Laboratory for High Speed Railway Construction*, *Central South University*, *Changsha*, *410075*, *China*
[3] *Department of Civil and Environmental Engineering*, *University of California*, *Berkeley*, *CA*, *USA*

(*Received January 16, 2019, Revised August 11, 2019, Accepted October 14, 2019*)

Abstract. This paper describes a study of the mapping relationship between the vertical deformation of bridge structures and rail deformation of high-speed railway, taking the interlayer interactions of the bridge subgrade CRTS II ballastless slab track system (HSRBST) into account. The differential equations and natural boundary conditions of the mapping relationship between the vertical deformation of bridge structures and rail deformation were deduced according to the principle of stationary potential energy. Then an analytical model for such relationship was proposed. Both the analytical method proposed in this paper and the finite element numerical method were used to calculate the rail deformations under three typical deformations of bridge structures and the evolution of rail geometry under these circumstances was analyzed. It was shown that numerical and analytical calculation results are well agreed with each other, demonstrating the effectiveness of the analytical model proposed in this paper. The mapping coefficient between bridge structure deformation and rail deformation showed a nonlinear increase with increasing amplitude of the bridge structure deformation. The rail deformation showed an obvious "following feature"; with the increase of bridge span and fastener stiffness, the curve of rail deformation became gentler, the track irregularity wavelength became longer, and the performance of the rail at following the bridge structure deformation was stronger.

Keywords: high-speed railway; bridge structure; analytical model; mapping relationship

1. Introduction

As indicated by the analysis of the bridge occupation ratios of 28 typical railways in current China as shown in Fig. 1, the average bridge occupation ratio is as high as 53%, and the maximum bridge occupation ratio is as high as 94.2%. This suggests that high-speed trains, which are now used in mass transit operations, cannot avoid high-density operation on bridges (either temporally or spatially) (He *et al*. 2017, Li *et al*. 2018, Jiang *et al*. 2019a). With the constant increase of the traffic and mileage of high-speed railway systems running through regions with special conditions (such as seismically active belts, foundation settlement, and extreme climates), bridge structures are inevitably subjected to all kinds of deformations like pier inclination, girder body fault and girder end rotation, bearing deformation, and so forth (Ju 2013, Cheng *et al*. 2016, Kang *et al*. 2017, Kun *et al*. 2018). Because of the deformation compatibility effect of the bridge subgrade ballastless track system, these accumulated residual deformations are mostly mapped onto rail surfaces, thus increasing the rail additional irregularity. When a train runs by at high speed, such the rail additional irregularity increases the excitation at the wheel-rail interface, intensifies train vibration through wheel-rail dynamic interactions, jeopardizes train safety and comfort, and ultimately affects its operational safety (Yau 2009, Sun *et al*. 2015, Wang *et al*. 2015, Arisoy and Erol 2018).

The rail geometric irregularity of bridges is one of the key factors influencing the running safety of high-speed trains. Studying the mechanism of interactions among different parts of bridge structures and revealing the mapping relationship between bridge structure deformation and rail deformation are of vital theoretical and practical significance for the comprehensive static and dynamic management of the operational safety of high-speed railway lines (Zhai *et al*. 2014, Jahangiri and Zakeri 2017). A long-term observation of pier settlement on a certain high-speed railway has been carried out by the Beijing Railway Bureau (Shi 2013). Adopting these settlement data (Shi 2013), Chen *et al*. (2015) presented a method to determine the safety threshold of bridge pier settlement in high-speed railways. An analytical expression of the mapping relationship between the pier settlement and rail deformation was derived theoretically for the unit slab track system, longitudinal connected ballastless track system and double block ballastless track-bridge system to determine the safety

*Corresponding author, Ph.D., Professor,
E-mail: zhouwangbao@163.com
[a] Ph.D. Student, E-mail: fylin119@csu.edu.cn
[b] Ph.D., Professor, E-mail: lzhjiang@csu.edu.cn
[c] Ph.D., E-mail: laizhipeng2016@163.com
[d] Ph.D. Student, E-mail: 64539211@qq.com

ISSN: 1229-9367 (Print), 1598-6233 (Online)

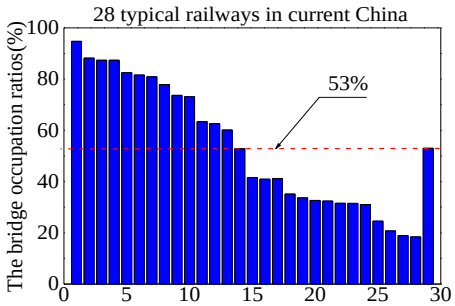

(a)

(b)

Fig. 1 The typical cartogram of the ratio of bridges to railway lines

threshold of bridge pier settlement in high-speed railway. Further, they analyzed the influence of multi-pier settlement on the train-track-bridge coupled dynamic system. The relationships between the pier settlement and the change amounts of vehicle dynamic indices were obtained. Results showed that the rail deformation caused by multi-pier settlement agrees well with the settlement data (Chen *et al*. 2018). The measurement results of track irregularity showed that the rail geometry is associated with the bridge deformation (Lee *et al*. 2012). Wei *et al*. (2011) conducted indoor tests and numerical simulation analysis to investigate the influence on girder end fasteners of the girder end rotation, girder body fault, and other deformations, and found the main factors influencing the magnitude of deformation and the additional force on fasteners. Cai *et al*. (2014) explored the relationship between the amplitude, scope and type of differential ground settlement and the regularity of the ballastless track system, based on finite element models of the girder-plate-entity spatial coupling of unit-plates and double-block ballastless tracks of high-speed railway. Gou *et al.* (2018a) presented an analytical model to analyze the mapping relationship between bridge lateral deformation and CRTS I track geometry of high-speed railway. Based on the rail deformation mechanisms, the deformation of track slab and rail at the locations of fasteners are analyzed, and the formulae of rail lateral deformation were derived and validated against a finite element model. Gou *et al*. (2019) also adopted the indoor experimental data of the fasteners force of the girder body fault which conducted by Wei *et al*. (2010) to verify the proposed analytical method. He *et al*. (2018), based on a finite element study for the subgrade bridge transition segment of CRTS Ⅲ slab track, analyzed the mapping relationship between differential settlement and rail deformation in the subgrade-bridge transition segments of high-speed railway. Furthermore, they developed a functional expression for that mapping relationship, using a least squares polynomial fit. Clearly, there are currently only quantitative studies on such mapping relationship. Specially the studies on the mapping relationship between the continuous girder bridge vertical deformation and rail deformation in HSRBST are rarely reported.

Thus, establishing the mapping relationship between the bridge structure vertical deformation and rail deformations of high-speed railway has vital theoretical significance and value for engineering applications. In this paper, the differential equations and natural boundary conditions of the mapping relationship between the vertical deformation of bridge structures and rail deformation were deduced according to the principle of stationary potential energy. Then an analytical model for such relationship was proposed. Both the analytical method proposed in this paper and the finite element numerical method were used to calculate the rail deformations under three typical deformations of bridge structures and analyze the evolution of rail geometry under these circumstances. The conclusions drawn in this paper provides a theoretical basis for developing a geometry model for high-speed railway lines, and lays a solid theoretical and scientific foundation to help guarantee the safe and efficient operation of high-speed railway.

2. Mapping relationship between bridge structure deformation and rail deformation

2.1 Basic assumptions

Taking HSRBST as an example, the girder bodies are firmly connected with track slabs and base plate via shear slots, shear studs, CA mortar layers, shear rebars and fastening-type lateral chock blocks. In the case of vertical deformation of the bridge structures in the system, the rail would experience following deformation under the tensile or compressive force of fasteners. To build a simplified model for the mapping relationship between bridge structure deformation and rail deformation, the following basic assumptions have been made (Biondi *et al*. 2005, Qiao *et al*. 2018):

(1) Due to the vertical confinement effect of shear slots, shear studs, CA mortar layers, shear rebars, fastening-type lateral chock blocks (used to limit the vertical displacement of base plates and track slab), and other interlayer components, it is assumed that both track slabs and base plate are coordinated with bridge girder body in terms of vertical deformation.

(2) The enough subgrade segment length is adopted to eliminate the boundary effect of rail, and the two ends of rail are simplified as simply supported boundaries in the model for mapping relationship.

(3) In the stress analysis of various structures, the origin of the vertical coordinate axis is set at the gravitational equilibrium position of each structure

before deformation and the effects of gravity are excluded from calculations.

(4) Given that the vertical bending stiffness of a bridge is far greater than the bending stiffness of a rail, the influence of rails on bridge structure deformation could be ignored.

(5) Assume that the vertical deformation curve, caused by the bearings or piers' deformation, of the continuous girder bridge and the simply supported girder bridge are cubic polynomials and linear polynomial, respectively.

(6) The connections between the rail and bridge are assumed to be evenly distributed and arranged along the center line of the rail according to the space between two fasteners.

2.2 Differential equations and boundary conditions of the mapping relationship

As shown in Fig. 2, the HSRBST was divided into nine parts from left to right. That is, the subgrade's left segment (I), the i ($i = 0,1,2,\dots$) span's left-side non-adjacent simply supported girder (II), left-side adjacent simply supported girder (III), the three-span continuous girders (IV, V, VI), the right-side adjacent simply supported girder (VII), the j($j = 0,1,2,\dots$) span's right-side non-adjacent simply supported girder ($VIII$), and the subgrade's right segment (IX). A local coordinate system at the left end of each part is used, and the deformation function of the rail was assumed to be $u(x)_{Rm}$ ($m = I,\dots,IX$), the deformation functions of left-side and right-side subgrade respectively to be $u(x)_{BI}$ and $u(x)_{BIX}$, and that of a bridge structure to be $u(x)_{Bm}$ ($m = II,\dots,VIII$).

The bending strain energy U_m of the rail can be expressed as

$$U_m = \frac{1}{2}\int_{L_m} E_{Rm}I_{Rm}(u''(x)_{Rm})^2\,dx \tag{1}$$

The elastic potential energy K_m of the fasteners can be expressed as

$$K_m = \frac{1}{2}\int_{L_m} k_m(u(x)_{Rm} - u(x)_{Bm})^2\,dx \tag{2}$$

Where, L_m ($m = I,\dots,IX$) represents the subgrade segment length for simply supported girder span and continuous girder span; k_m, E_{Rm}, I_{Rm} ($m = I,\dots,IX$) represent the fastener stiffnesses, Young's modulus, and the second moment of inertia for the cross-sections of parts $I,\dots,IX$, respectively.

The total potential energy of the HSRBST can be expressed as

$$\Pi = \sum_{m=I}^{IX}(U_m + K_m) \tag{3}$$

According to the principle of stationary potential energy $\delta\Pi = 0$ (Podworna 2017, Jiang *et al*. 2018, 2019b, Feng *et al*. 2019), the differential equation and natural boundary conditions of the mapping relationship between the vertical deformation of the bridge structures and the rail deformation can be expressed as

$$E_{Rm}I_{Rm}u(x)^{IV}_{Rm} + k_m u(x)_{Rm} = k_m u(x)_{Bm} \tag{4}$$

$$E_{Rm}I_{Rm}u''(x)_{Rm}\delta u'(x)_{Rm}\big|_{x=L_m} = 0 \tag{5}$$

$$E_{Rm}I_{Rm}u'''(x)_{Rm}\delta u(x)_{Rm}\big|_{x=L_m} = 0 \tag{6}$$

2.3 Solution of the differential equation for the mapping relationship

Let

$$\lambda_m = \sqrt[4]{\frac{k_m}{4E_{Rm}I_{Rm}}} \tag{7}$$

The homogeneous solution of (4) can be expressed as

$$\begin{aligned} u(x)^h_{Rm} = {} & A_{Rm}\,ch\,\lambda_m x\cos\lambda_m x \\ & + B_{Rm}\mathrm{ch}\lambda_m x\sin\lambda_m x \\ & + C_{Rm}\mathrm{sh}\lambda_m x\cos\lambda_m x \\ & + D_{Rm}\mathrm{sh}\lambda_m x\sin\lambda_m x \end{aligned} \tag{8}$$

Where, A_{Rm}, B_{Rm}, C_{Rm}, D_{Rm} are all constant coefficients.

It could be known from the assumption (5) that $u(x)_{Bm}$ is a cubic polynomial, and that the particular solution of Eq. (4) is $u(x)_{Bm}$, so the general solution of Eq. (4) becomes

$$u(x)_{Rm} = u(x)^h_{Rm} + u(x)_{Bm} \tag{9}$$

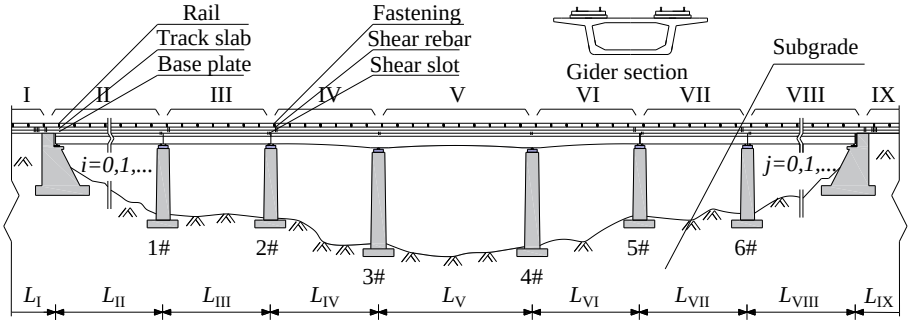

Fig. 2 The structural map of HSRBST

The simply supported boundary conditions of the two ends of the rail can be respectively expressed as

$$u''(x)_{RI}\big|_{x=0} = 0 \tag{10}$$

$$u(x)_{RI}\big|_{x=0} = 0 \tag{11}$$

$$u''(x)_{RIX}\big|_{x=L_{IX}} = 0 \tag{12}$$

$$u(x)_{RIX}\big|_{x=L_{IX}} = 0 \tag{13}$$

According to the displacement compatibility of the rail

$$u(x)_{RI}\big|_{x=L_I} = u(x)_{RII}\big|_{x=0} \tag{14}$$

$$u'(x)_{RI}\big|_{x=L_I} = u'(x)_{RII}\big|_{x=0} \tag{15}$$

$$u''(x)_{RI}\big|_{x=L_I} - u''(x)_{RII}\big|_{x=0} = 0 \tag{16}$$

$$u'''(x)_{RI}\big|_{x=L_I} - u'''(x)_{RII}\big|_{x=0} = 0 \tag{17}$$

$$\vdots$$

$$u(x)_{RVIII}\big|_{x=L_{VIII}} = u(x)_{RIX}\big|_{x=0} \tag{18}$$

$$u'(x)_{RVIII}\big|_{x=L_{VIII}} = u'(x)_{RIX}\big|_{x=0} \tag{19}$$

$$u''(x)_{RVIII}\big|_{x=L_{VIII}} - u''(x)_{RIX}\big|_{x=0} = 0 \tag{20}$$

$$u'''(x)_{RVIII}\big|_{x=L_{VIII}} - u'''(x)_{RIX}\big|_{x=0} = 0 \tag{21}$$

Substituting Eq. (8) into the boundary conditions expressed in Eqs. (10)-(21), and let

$$\begin{cases} c_m = ch\,\lambda_m L_m \\ q_m = cos\,\lambda_m L_m \\ s_m = \mathrm{sh}\lambda_m L_m \\ p_m = sin\,\lambda_m L_m \end{cases} \tag{22}$$

It is therefore known that

$$\begin{bmatrix} \boldsymbol{M}_I & \mathbf{0} & \mathbf{0} & \mathbf{0} & \mathbf{0} & \mathbf{0} & \mathbf{0} & \mathbf{0} & \mathbf{0} \\ \boldsymbol{M}_{SI} & \boldsymbol{M}_{TII} & \mathbf{0} & \mathbf{0} & \mathbf{0} & \mathbf{0} & \mathbf{0} & \mathbf{0} & \mathbf{0} \\ \mathbf{0} & \boldsymbol{M}_{SII} & \boldsymbol{M}_{TIII} & \mathbf{0} & \mathbf{0} & \mathbf{0} & \mathbf{0} & \mathbf{0} & \mathbf{0} \\ \mathbf{0} & \mathbf{0} & \boldsymbol{M}_{SIII} & \boldsymbol{M}_{TIV} & \mathbf{0} & \mathbf{0} & \mathbf{0} & \mathbf{0} & \mathbf{0} \\ \mathbf{0} & \mathbf{0} & \mathbf{0} & \boldsymbol{M}_{SIV} & \boldsymbol{M}_{TV} & \mathbf{0} & \mathbf{0} & \mathbf{0} & \mathbf{0} \\ \mathbf{0} & \mathbf{0} & \mathbf{0} & \mathbf{0} & \boldsymbol{M}_{SV} & \boldsymbol{M}_{TVI} & \mathbf{0} & \mathbf{0} & \mathbf{0} \\ \mathbf{0} & \mathbf{0} & \mathbf{0} & \mathbf{0} & \mathbf{0} & \boldsymbol{M}_{SVI} & \boldsymbol{M}_{TVII} & \mathbf{0} & \mathbf{0} \\ \mathbf{0} & \mathbf{0} & \mathbf{0} & \mathbf{0} & \mathbf{0} & \mathbf{0} & \boldsymbol{M}_{SVII} & \boldsymbol{M}_{TVIII} & \mathbf{0} \\ \mathbf{0} & \mathbf{0} & \mathbf{0} & \mathbf{0} & \mathbf{0} & \mathbf{0} & \mathbf{0} & \boldsymbol{M}_{SVIII} & \boldsymbol{M}_{TIX} \\ \mathbf{0} & \mathbf{0} & \mathbf{0} & \mathbf{0} & \mathbf{0} & \mathbf{0} & \mathbf{0} & \mathbf{0} & \boldsymbol{M}_{IX} \end{bmatrix} \begin{Bmatrix} \boldsymbol{C}_1 \\ \boldsymbol{C}_2 \\ \boldsymbol{C}_3 \\ \boldsymbol{C}_4 \\ \boldsymbol{C}_5 \\ \boldsymbol{C}_6 \\ \boldsymbol{C}_7 \\ \boldsymbol{C}_8 \\ \boldsymbol{C}_9 \\ \boldsymbol{C}_{10} \end{Bmatrix} = \begin{Bmatrix} \boldsymbol{U}_1 \\ \boldsymbol{U}_2 \\ \boldsymbol{U}_3 \\ \boldsymbol{U}_4 \\ \boldsymbol{U}_5 \\ \boldsymbol{U}_6 \\ \boldsymbol{U}_7 \\ \boldsymbol{U}_8 \\ \boldsymbol{U}_9 \\ \boldsymbol{U}_{10} \end{Bmatrix} \tag{23}$$

Where

$$\boldsymbol{M}_I = \begin{bmatrix} 1 & 0 & 0 & 0 \\ 0 & 0 & 0 & 1 \end{bmatrix} \tag{24}$$

$$\boldsymbol{M}_{Tm} = \begin{bmatrix} -1 & 0 & 0 & 0 \\ 0 & -\lambda_m & -\lambda_m & 0 \\ 0 & 0 & 0 & -2\lambda_m^2 \\ 0 & -\lambda_m^3 & \lambda_m^3 & 0 \end{bmatrix}, m = II, \ldots, IX \tag{25}$$

$$\boldsymbol{M}_{Sm} = \begin{bmatrix} c_m q_m & c_m p_m & s_m q_m & s_m p_m \\ \lambda_m\left(s_m q_m - c_m p_m\right) & \lambda_m\left(c_m q_m + s_m p_m\right) & -\lambda_m\left(c_m q_m - s_m p_m\right) & \lambda_m\left(s_m q_m + c_m p_m\right) \\ -2\lambda_m^2 s_m p_m & 2\lambda_m^2 s_m q_m & -2\lambda_m^2 c_m p_m & 2\lambda_m^2 c_m q_m \\ -2\lambda_m^3\left(s_m q_m + c_m p_m\right) & 2\lambda_m^3\left(c_m q_m - s_m p_m\right) & -2\lambda_m^3\left(s_m p_m + c_m q_m\right) & 2\lambda_m^3\left(s_m q_m - c_m p_m\right) \end{bmatrix}, \quad m = I, \ldots, VIII \tag{26}$$

$$\boldsymbol{M}_{IX} = \begin{bmatrix} c_{IX} q_{IX} & c_{IX} p_{IX} & s_{IX} q_{IX} & s_{IX} p_{IX} \\ -2\lambda_{IX}^2 s_{IX} p_{IX} & 2\lambda_{IX}^2 s_{IX} q_{IX} & -2\lambda_{IX}^2 c_{IX} p_{IX} & 2\lambda_{IX}^2 c_{IX} q_{IX} \end{bmatrix} \tag{27}$$

$$\boldsymbol{C}_I = \begin{Bmatrix} A_I \\ B_I \end{Bmatrix}, \qquad \boldsymbol{C}_{m+1} = \begin{Bmatrix} C_m \\ D_m \\ A_{m+1} \\ B_{m+1} \end{Bmatrix}, \quad m = I, \ldots, VIII, \qquad \boldsymbol{C}_{IX+1} = \begin{Bmatrix} C_{IX} \\ C_{IX} \end{Bmatrix} \tag{28}$$

$$\boldsymbol{U}_I = \begin{Bmatrix} -u(0)_{RI} \\ -u''(0)_{RI} \end{Bmatrix}, \qquad \boldsymbol{U}_m = \begin{Bmatrix} u(0)_{Rm} - u(L_{m-1})_{R(m-1)} \\ u'(0)_{Rm} - u'(L_{m-1})_{R(m-1)} \\ u''(0)_{Rm} - u''(L_{m-1})_{R(m-1)} \\ u'''(0)_{Rm} - u'''(L_{m-1})_{R(m-1)} \end{Bmatrix}, \quad m = II, \ldots, IX, \qquad \boldsymbol{U}_{IX+1} = \begin{Bmatrix} -u(L_{IX})_{RIX} \\ -u''(L_{IX})_{RIX} \end{Bmatrix} \tag{29}$$

Solving the algebraic equation set (23) leads to a coefficient matrix$\{\boldsymbol{C}\}$, which can be substituted into (9) to obtain an analytical expression for the mapping relationship between the vertical deformation of the bridge structures and the rail geometric deformation.

3. Analysis of examples

To verify the correctness and practicality of the analytical method proposed in this paper, three typical vertical deformations were introduced in this paper as shown in Fig. 3 as examples (Gou *et al*. 2018b). These are the continuous girder piers' differential settlement, girder end rotation and simply supported girder body fault. The proposed analytical method (MA Model) and the ANSYS finite element numerical method (FE Model) were used to calculate and compare the mapping deformation of rail in HSRBST under three typical vertical deformations. In FE Model, the BEAM188 element in ANSYS was used to simulate the continuous girder bridge, simply supported girder bridge and each layer of track structure, respectively; the COMBIN14 spring element were used to simulate the subgrade, the fasteners and other interlayer connections between the track structure and the bridge and between the track structure and the subgrade; the MPC184 element was used to simulate the rigid constraint between the master and slave nodes; and the bearings or piers' deformation were

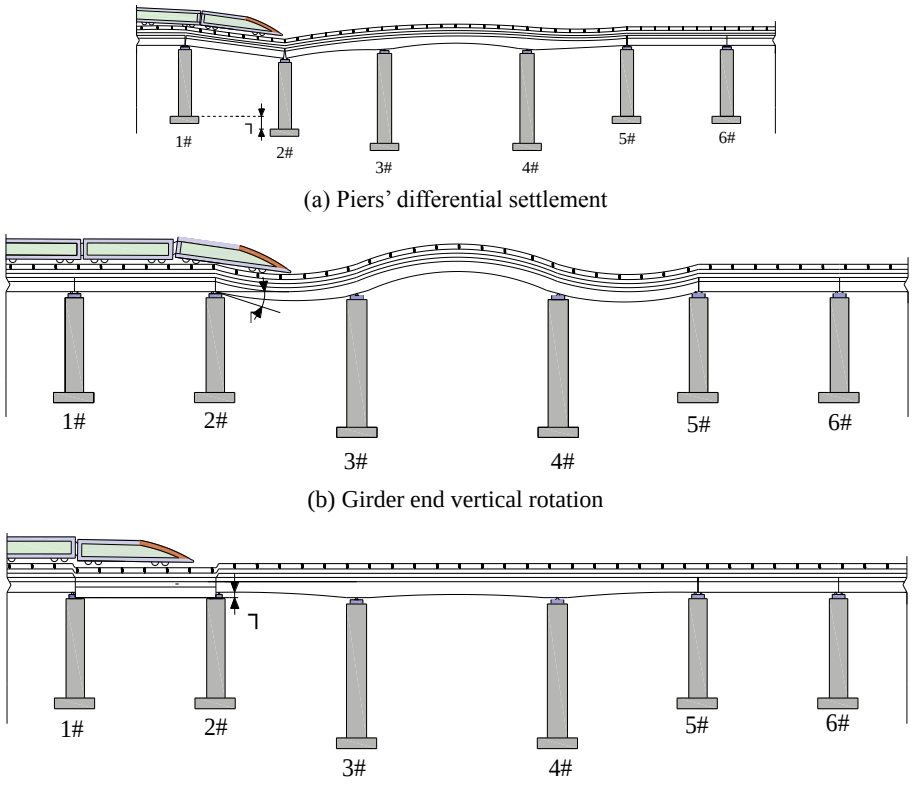

(a) Piers' differential settlement

(b) Girder end vertical rotation

(c) Girder vertical body fault

Fig. 3 Three typical vertical deformations of bridge structure

simulated by the corresponding displacement constraints.

For the numerical scheme, firstly, apply the corresponding forced displacement to the bridge structure (pier settlement, girder body fault or girder end rotation, etc); then, define the displacement convergence criteria as 0.05 and the substeps as automatic time step; finally, the Modal analysis was adopted first followed by the Static analysis (Zhou *et al*. 2013, 2017). The flowchart of solving the proposed analytical method is shown in Fig. 4. The main parameters of the calculation model are as follows: the simply supported girder span: 32 m; the spans of three-span continuous girders: 48 m + 80 m + 48 m; the subgrade segment lengths at the both ends: 200 m (Toyooka *et al*. 2005); the rail parameters: actual section parameters of seamless rail (60 kg/m); fastener stiffness: 6e7 N/m; concrete strength grade of track slab: C55; concrete strength grade of base plate: C40; concrete strength grade of girder body: C50; concrete strength grade of pier: C30. Fig. 5 shows the schematic diagram of FE model for the HSRBST (Lai *et al*. 2018).

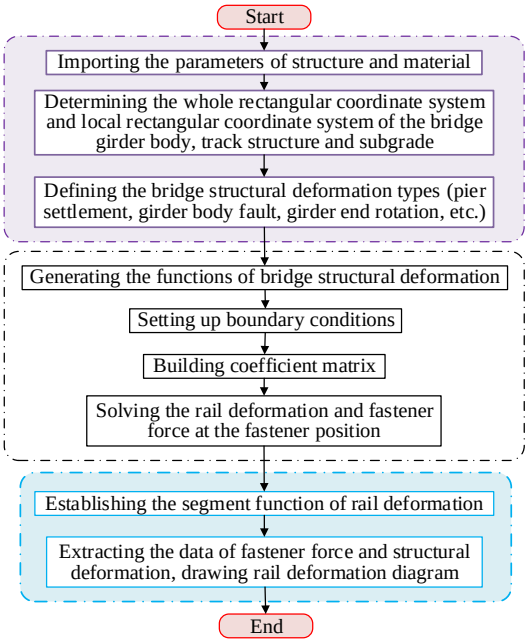

Fig. 4 The flowchart of solving the proposed analytical method

3.1 Study on the mapping relationship for pier settlement-rail deformations

As shown in Fig. 3(a), taking the settlement deformation of 2# pier as an example, the settlement of 2# pier is assumed asΔ. According to assumption (5), the vertical deformation of the simply supported girder body connected with the 2# pier, as a result of 2# pier settlement, can be expressed as

$$u(x)_{BIII} = \frac{\Delta}{L_{II}} x \tag{30}$$

According to assumption (5), the simply supported girder bodies and subgrade not connect with 2# pier can be

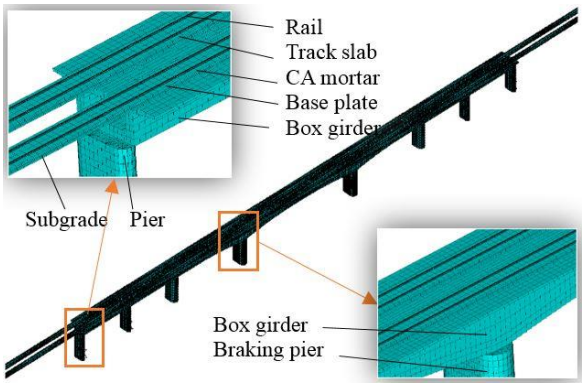

Fig. 5 Schematic diagram of FE model of HSRBST

expressed as

$$u(x)_{BI} = 0, \quad u(x)_{BIX} = 0 \tag{31}$$

$$u(x)_{BII} = 0, \quad u(x)_{BVII} = 0, \quad u(x)_{BVIII} = 0 \tag{32}$$

The function of the continuous girder bridge deformation induced by the pier's settlement is a cubic polynomial of x, the deformation functions of three-span continuous girders can be given as

$$u(x)_{BIV} = \frac{1}{E_{IV}I_{IV}} \begin{pmatrix} -\frac{F_1}{6}x^3 \\ +A_1x + B_1 \end{pmatrix}, \quad x \in [0, L_{IV}] \tag{33}$$

$$u(x)_{BV} = \frac{1}{E_V I_V} \begin{pmatrix} -\frac{(F_1+F_2)}{6}x^3 \\ -\frac{F_1 L_{IV}}{2}x^2 \\ +A_2x + B_2 \end{pmatrix}, \quad x \in [0, L_V] \tag{34}$$

$$u(x)_{BVI} = \frac{1}{E_{VI}I_{VI}} \begin{pmatrix} \frac{F_4}{6}x^3 \\ -\frac{F_4 L_{IV}}{2}x^2 \\ +A_3x + B_3 \end{pmatrix}, \quad x \in [0, L_{VI}] \tag{35}$$

Where, $A_1, B_1, C_1, D_1, F_1, F_2, F_3, F_4$ are the coefficients of the function for continuous girder deformation.

In case of settlement of the other piers, the analysis process is the same as that of 2# pier.

According to the prescribed limit of the bridge structure deformation for high-speed railways, the limit of the adjacent pier settlement difference of a ballastless track bridge under constant loads is 5 mm (Ministry of Railways 2014). The FE Model and MA Model are used to calculate the rail deformations caused by the settlement of 5 mm of the 2# pier and the 3# pier; the calculations' results are shown in Fig. 6. To discuss the deformation scope and deformation degree of the rail for the case of the pier's settlement, the region where the rail deformation exceeded 0.01 mm is defined as the mapping region for rail deformation (Gou *et al*. 2018a). The mapping regions of the rail deformation caused by a settlement of 5 mm of the 2# pier and the 3# pier were calculated. Those calculation results are shown in Table 1, where M_{d+} and M_{d-} respectively represent the maximum upward and downward deformations of the rails, P_s and P_e respectively represent the starting and endpoint positions of the mapping deformations, and L_r represents the mapping region of the rails' deformation.

According to Fig. 6 and Table 1, the results for the curve and mapping region of the rail's deformation were calculated using FE Model and MA Model. These results agreed well, which verified the correctness of the MA Model. The results indicated that either of these methods can be used to solve the mapping relationship between the

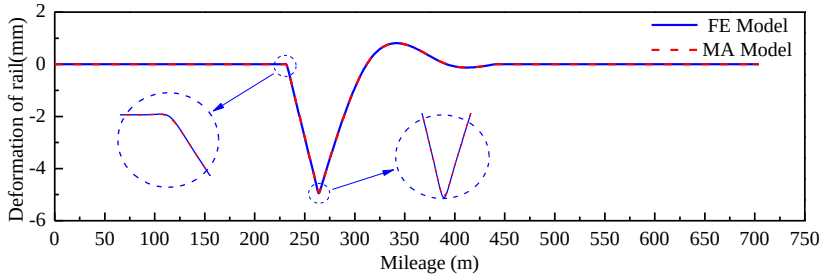

(a) 2#pier settlement

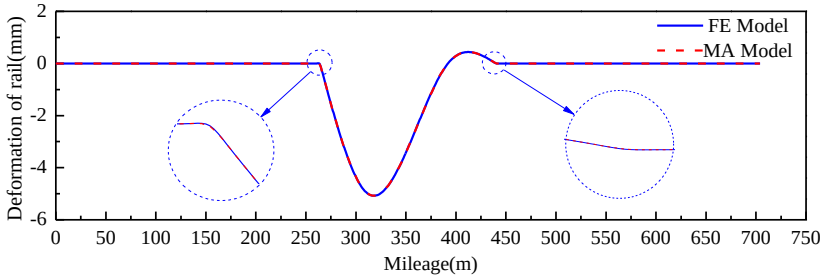

(b) 3# pier settlement

Fig. 6 Rail deformation diagram for the pier settlement of 5 mm

Table 1 Rail deformation region data for the pier settlement of 5 mm

Pier settlement	Calculation method	P_s (m)	L_r (m)	P_e (m)	M_{d+} (mm)	M_{d-} (mm)
2#pier	FE Model	229.000	211.000	440.000	0.809	-4.947
	MA Model	229.000	211.000	440.000	0.808	-4.931
	Relative deviation	0.000%	0.000%	0.000%	0.096%	0.300%
3#pier	FE Model	261.000	181.000	442.000	0.438	-5.077
	MA Model	261.000	181.000	442.000	0.439	-5.078
	Relative deviation	0.000%	0.000%	0.000%	0.160%	0.001%

Table 2 Rail deformation region data for the girder end rotation of 1‰ rad

Calculation method	P_s (m)	L_r (m)	P_e (m)	M_{d+} (mm)	M_{d-} (mm)
FE Model	261.000	178.500	439.500	4.312	-8.407
MA Model	261.000	178.500	439.500	4.330	-8.417
Relative deviation	0.000%	0.000%	0.000%	-0.430%	0.110%

piers' settlement and the rails' deformation in HSRBST. Also, relative to the FE Model, MA Model could more clearly express the relationships between various parameters' influence on rail deformation and could significantly shorten the required calculation time. In the adjacent region of pier settlement, rail deformation presents a trend of local upward first, and soon sinks. Such the local upward region is bound to increase the wheel-rail force when the train runs into the settlement region, so close attention should be paid to this aspect during design for operational safety. For the case of the 2# pier settlement, the maximum upward deformation of the rail occurred on the 3# pier, while the maximum downward deformation occurred on the 2# pier; in the case of the 3# pier settlement, the maximum upward deformation of the rail occurred in the middle of the 4# pier and the 5# pier, while the maximum downward deformation occurred on the 3# pier. According to the assumption (5), the simply supported girder deformation could be seen as rigid body deformation. Because of the high compressive stiffness of fasteners and linear rigid body deformation of the simply supported girder, the rail deformation caused by the downward traction of fasteners would have several "break angle" at the points of pier settlement, as shown in Fig. 6(a). The rail deformation curves actually varied smoothly and continuously when going in and out of the "break angle" region,which looks as a little sharp because of the drawing proportion.

3.2 Study on the mapping relationship for girder end rotation-rail deformations

As shown in Fig. 3(b), according to the prescribed limit of girder end vertical rotation for high-speed railway bridges, the magnitude of the girder end vertical rotation was set as 1‰ rad, (Sun *et al.* 2016); The rest of girder body of bridge span did not have vertical rotation deformation. The FE Model and MA Model were used to calculate the rail deformation for a girder end rotation of 1‰rad; see calculation results in Fig. 7 and the data on the mapping region for rail deformation shown in Table 2. As can be seen from Fig. 7 and Table 2, in the case of girder end vertical rotation deformation, the results for the rail deformation curve and rail deformation region calculated by FE Model and MA Model agreed well. In the rotation deformation region, the rail followed the girder body's deformation; the rail deformation decreased rapidly with increase of distance from the deformation area. The left-side rail geometry in the deformation region presented a change trend of uplifting first and sagging afterwards; the right-side rail geometry in the deformation region showed a trend towards sagging first and uplifting afterwards, followed by a gentle downward transition. In the rotation deformation region, rail deformation followed approximately

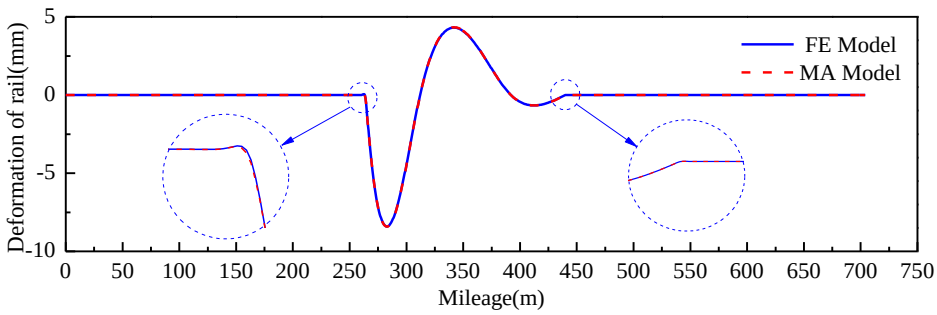

Fig. 7 Rail deformation diagram for the girder end rotation of 1‰ rad

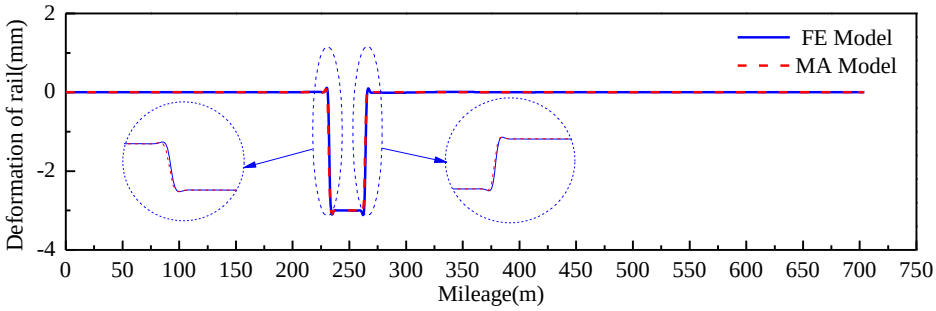

Fig. 8 Rail deformation diagram for the girder vertical body fault of 3 mm

Table 3 Rail deformation region data for the girder vertical body fault of 3 mm

Calculation method	P_s (m)	L_r (m)	P_e (m)	M_{d+} (mm)	M_{d-} (mm)
FE Model	228.000	40.125	268.125	0.101	-3.101
MA Model	228.000	40.125	268.125	0.097	-3.097
Relative deviation	0.000%	0.000%	0.000%	3.120%	0.090%

a cosine wave shape, with a maximum deformation at the wave trough of 8.4 mm and a maximum deformation at the wave crest of 4.3 mm. The maximum deformation exceeded the prescribed limit (5 mm) of bridge structure deformations for high-speed railway, suggesting that girder end rotation exerts a significant influence on rail deformation and that close attention should be paid to this aspect of deformation by engineering designers.

3.3 Study on the mapping relationship for girder body fault-rail deformations

As shown in Fig. 3(c), according to the prescribed limit for girder body fault of high-speed railway bridges, the fault magnitude was set to 3 mm; the rest of the girder body of bridge span does not have vertical fault deformation. The FE Model and MA Model were used to calculate the rail deformation upon a girder body vertical fault of 3mm; see calculation results in Fig. 8 and Table 3.

As can be seen from Fig. 8 and Table 3, in the case of girder body vertical fault, the results for the curve and mapping region of the rails' deformation calculated by the FE Model and MA Model agreed well, and the overall deformation of rail in the deformation region had bilateral symmetry which further demonstrated the effectiveness of the MA Model. In the region of girder body vertical fault, the rails' deformation increased rapidly, and the maximum deformation of rail was approximately equal to that of girder body. With increase of distance from the fault region, the rails' deformation quickly dropped to zero, and between

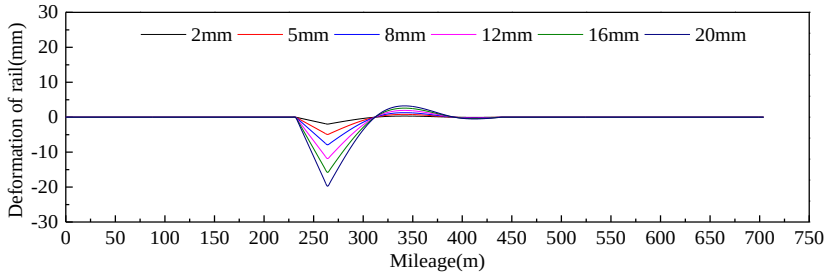

(a) 2#pier settlement

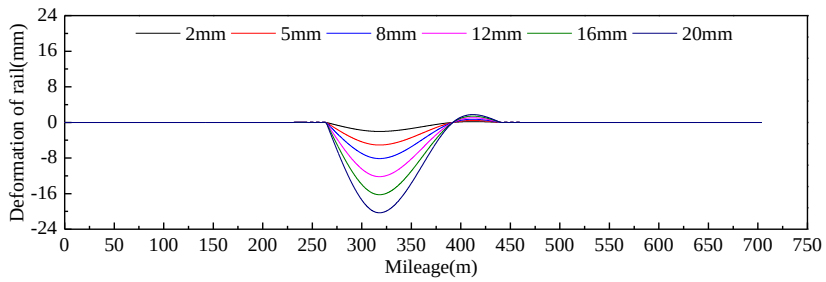

(b) 3# pier settlement

Fig. 9 Rail deformation diagram under different amplitudes of pier settlement

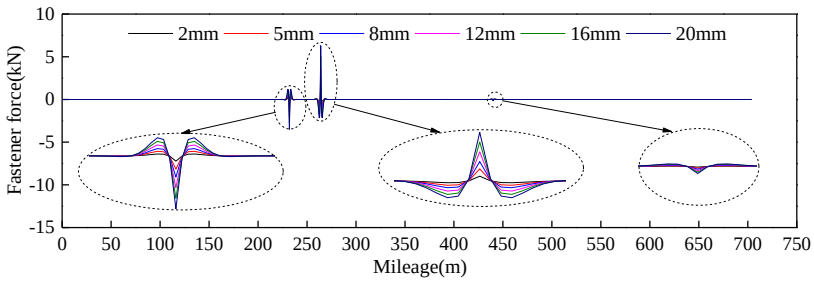

(a) 2#pier settlement

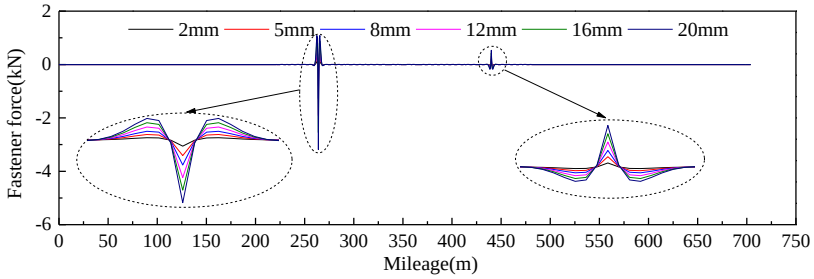

(b) 3# pier settlement

Fig. 10 Fasteners internal force distribution under different amplitudes of pier settlement

the maximum and minimum rail deformations there was only a tiny local uplift transition to approximately a half-sine wave whose wave crest value did not exceed 0.2 mm. As a result, upon entry into and exit from the fault region, the curve of the rails' deformation experienced abrupt oscillations which would be detrimental to the running safety and ride comfort of high-speed trains.

4. Study on the evolution law of bridge structure deformations to rail deformations

4.1 Influence of the amplitude of pier settlement on rail deformation

By changing the amplitudes of the 2# pier and 3# pier settlements and respectively setting them as 2 mm, 5 mm, 8 mm, 12 mm, 16 mm and 20 mm, the rail deformation curves under different amplitudes of pier settlement were calculated, and the influence of the amplitude of pier settlement on rail deformation was analyzed. Figs. 9-10 show the calculated results for rail deformation and fasteners' internal force distribution under different amplitudes of pier settlement.

As can be seen from Figs. 9-10, for the case of pier settlement, the rail and girder body deformations maintained the following features: the state of deformation of the rails was closely related to the state of stress of the fasteners, and both rail deformations and fastener internal forces increased significantly with increased amplitude of the piers' settlement: the fastener internal forces induced by the piers' settlement was concentrated on both sides of the centerline of the girder crevices. For the case of the 2# pier settlement, the fastener internal forces in the vicinity of the girder crevices on the 2# pier and the 1# pier all showed relatively significant fluctuations, and peak internal forces

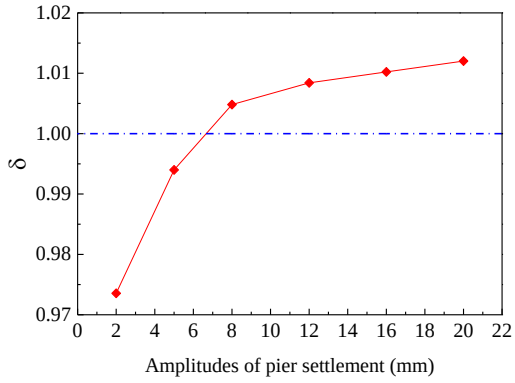

(a) 2#pier

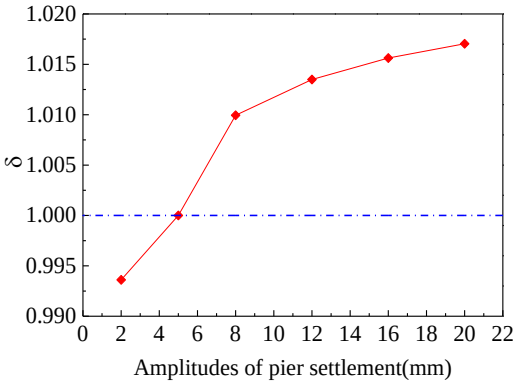

(b) 3#pier

Fig. 11 Relationship between amplitudes of pier settlement and mapping coefficient

were as high as 6 kN. In the case of 3# pier, the fastener internal forces around the girder crevices on the 3# pier also showed relatively significant fluctuations, and peak internal forces were as high as 3.5 kN; the fastener internal forces

around the girder crevices on the 5# pier fluctuated slightly, and peak internal forces were below 1 kN.

To quantitatively describe the degree of mapping from bridge structure deformation to rail deformation, a mapping coefficient δ was introduced. This mapping coefficient is the ratio of the length of rail deformation region L_r to the length of girder body deformation region L_b

$$\delta = \frac{L_r}{L_b} \tag{36}$$

Fig. 11 shows the changes of the mapping coefficient under different amplitudes of the 2# pier and 3# piers' settlement. Clearly, with the increased amplitude of the piers' settlement, the mapping coefficient first increased and then tended to stabilize, which indicates that the amplitude of the rails' settlement presents a nonlinear trend of gradually slowing growth with the increased amplitude of the piers' settlement. When the amplitude of the 2# pier's settlement was less than 7 mm and that of the 3# pier settlement was less than 5 mm, the mapping coefficient was less than 1. These results suggest that, because of both the deformation coordination effects of the track system's interlayer fasteners and the vertical bending stiffness of the rail itself, the mapping region length of the rails' deformation was less than the corresponding length of the deformation of the girder bodies. With the increased amplitude of the piers' settlement, the mapping coefficient gradually exceeded 1. This suggests that the local unwarping of the rail at the edge of region of settlement resulted in the diffusion to some extent of the rails' deformation relative to the bridge, and that the amplitude of such local unwarping also gradually increased with the increasing of pier settlement.

4.2 Influence of the amplitude of the girder end rotation on rail deformation

To study the influence of the amplitude of the girder end vertical rotation on rail deformations, the rail deformation was calculated after setting the amplitude of the vertical rotation of girder end of the continuous girder as 0.2‰ rad, 0.4‰ rad, 0.6‰ rad, 0.8‰ rad, 1.0‰ rad and 1.2‰ rad. This is shown in the calculated results for the mapping relationship between fastener internal forces and rail deformations in Figs. 12-14. Clearly, under different amplitudes for girder end vertical rotation, the rail geometry was always consistent with the morphology of girder body deformations; the extremely non-uniform fastener internal forces distribution, as induced by girder end vertical rotation, was mainly concentrated in the vicinity of the 2# pier. With increased amplitude of the girder end rotation, both rail deformation and fastener internal forces increased significantly. For the girder body under investigation in the deformation region, the mapping coefficient of the rail deformation increased with increasing girder end vertical rotation and was always greater than 1; this suggests that the length of the rail deformation region induced by the girder end vertical rotation was relatively large.

4.3 Influence of the amplitude of the girder body fault on rail deformation

To study the influence of the amplitude of the girder body vertical fault on the rail deformation, the rail deformation was calculated after setting the amplitude of girder body vertical fault as 0.5 mm, 1.0 mm, 2.0 mm, 3.0 mm, 4.0 mm and 5.0 mm; see the calculation results for the mapping relationship between the fastener internal forces distribution and the rail deformation in Figs. 15-17. Under

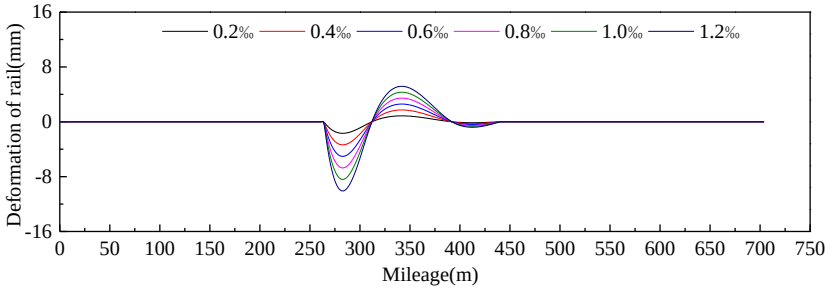

Fig. 12 Rail deformation diagram under different amplitudes of girder end vertical rotation

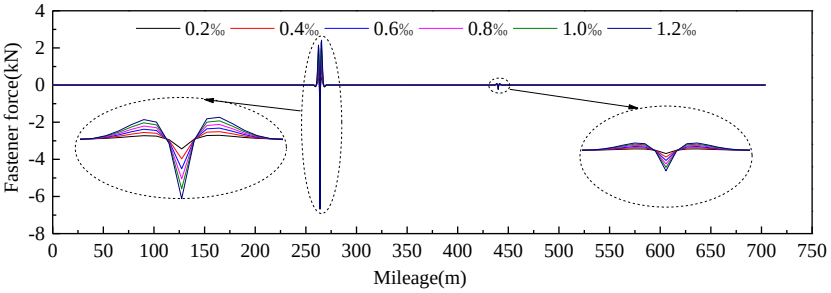

Fig. 13 Fastener internal force distribution under different amplitudes of girder end vertical rotation

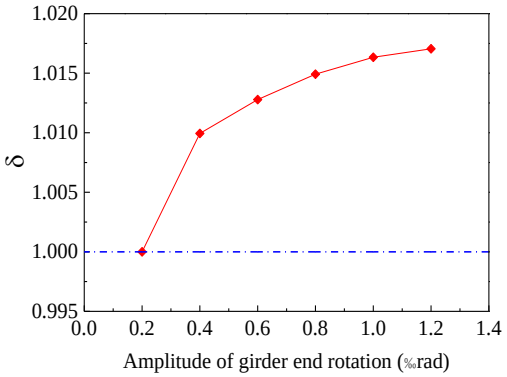

Fig. 14 Relationship between girder end vertical rotation and mapping coefficient

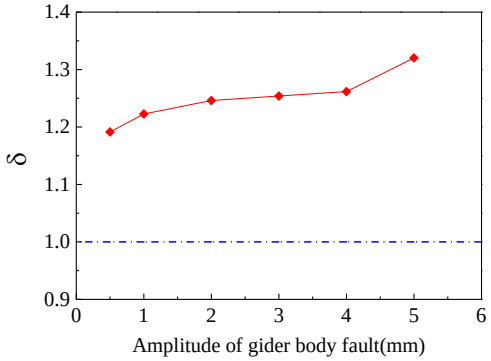

Fig. 15 Relationship between girder body vertical fault and mapping coefficient

different amplitudes of vertical fault, rail geometry always maintained a clear consistency with the morphology of girder body deformation in the faults' deformation region. With the increase of the amplitude of vertical fault, both rails' deformation and fastener internal forces gradually increased. When the amplitude of girder body fault exceeded 1mm, the fastener internal forces on the two ends of the girder bodies reached 26.0 kN and 26.0 kN, which exceeded the rated fastening toe load (15 kN) of the WJ-8 fasteners commonly used in China. Within the selected amplitude for vertical fault, the mapping coefficient of the rails' deformation was uniformly greater than 1, suggesting that the length of rails' region of deformation was uniformly greater than that of the girder body deformation. Thus, the rail deformation induced by girder body fault cannot be ignored.

4.4 Influence of fasteners' stiffness on rail deformation

As key components of the interlayer connection of the track system, fasteners exert a significant influence on rails' deformation. To explore the influence of fastener stiffness on rail deformation, the rails' deformations that were induced by pier settlement, girder body fault, and girder end rotation were calculated after setting fastener stiffness as 25 kN/mm, 45 kN/mm, 60 kN/mm, 75 kN/mm and 90 kN/mm; see calculation results in Tables 4-5 and Figs. 18-21.

As can be seen in Table 4 and Figs.18-19, when fastener stiffness was less than 45 kN/mm, with the increase of the vertical stiffness of the fasteners, the mapping region length and the mapping coefficient of the rails' deformation as

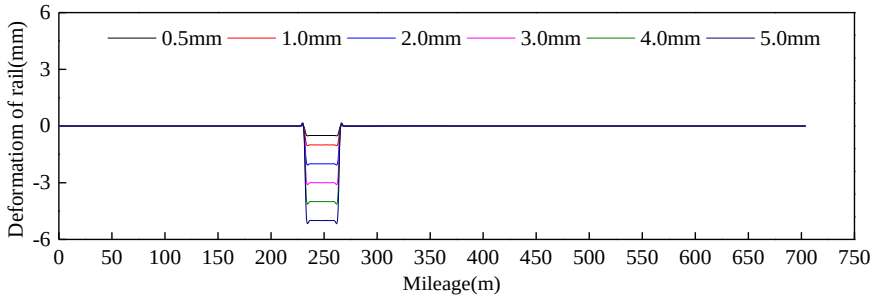

Fig. 16 Rail deformation diagram under different amplitudes of girder body vertical fault

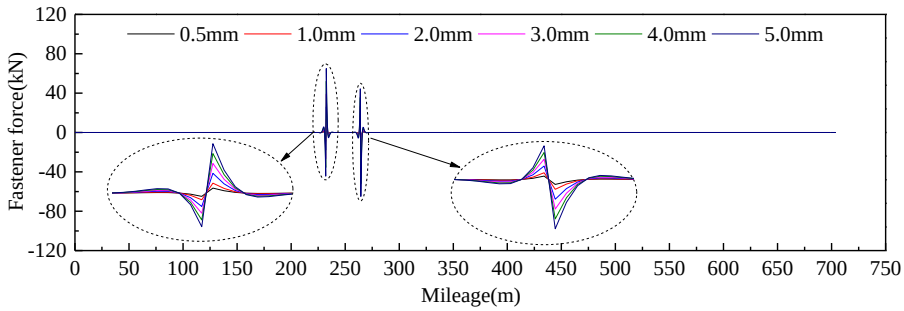

Fig. 17 Fastener internal force distribution under different amplitudes of girder body vertical fault

Table 4 Rail deformation region data for pier settlement under different fasteners stiffness

Rail deformation	Fasteners' stiffness (kN/mm)									
	2# pier settlement of 5mm					3# pier settlement of 5mm				
	25	45	60	75	90	25	45	60	75	90
L_r (m)	208.38	206.75	206.75	206.75	206.63	176.25	176.00	176.00	175.88	175.88
δ	1.002	0.994	0.994	0.994	0.993	1.001	1.000	1.000	0.999	0.999
M_{d-} (mm)	-4.919	-4.931	-4.936	-4.940	-4.943	-5.077	-5.077	-5.077	-5.077	-5.077
M_{d+} (mm)	0.809	0.809	0.809	0.809	0.809	0.439	0.439	0.439	0.439	0.439

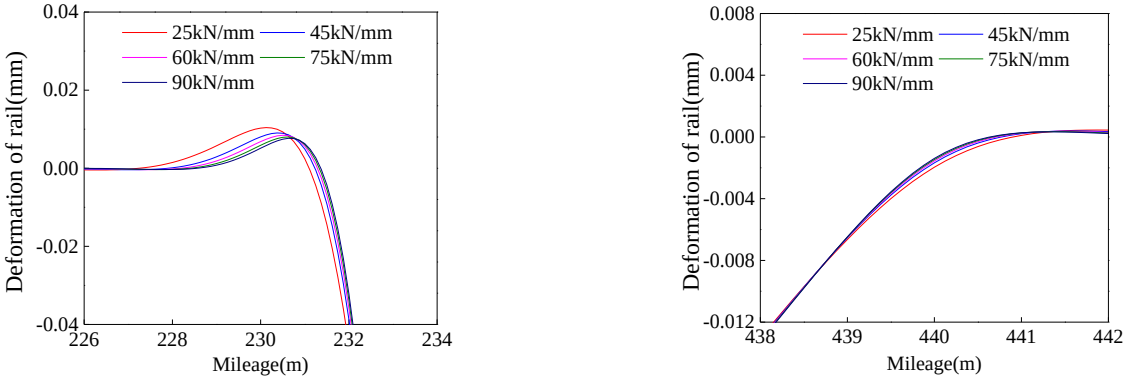

(a) The place of # 1 pier (b) The place of # 5 pier

Fig. 18 Effect of fastener stiffness on rail deformation for 2#pier settlement of 5 mm

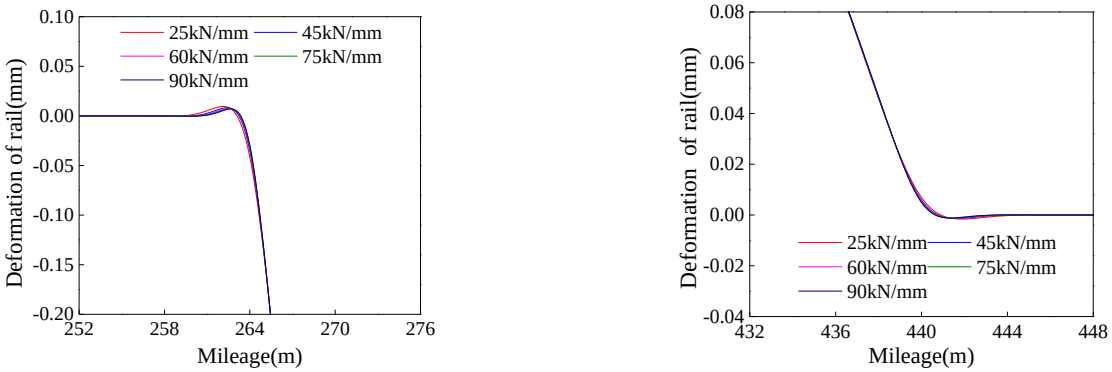

(a) The place of # 2 pier (b) The place of # 5 pier

Fig. 19 Effect of fastener stiffness on rail deformation for 3#pier settlement of 5 mm

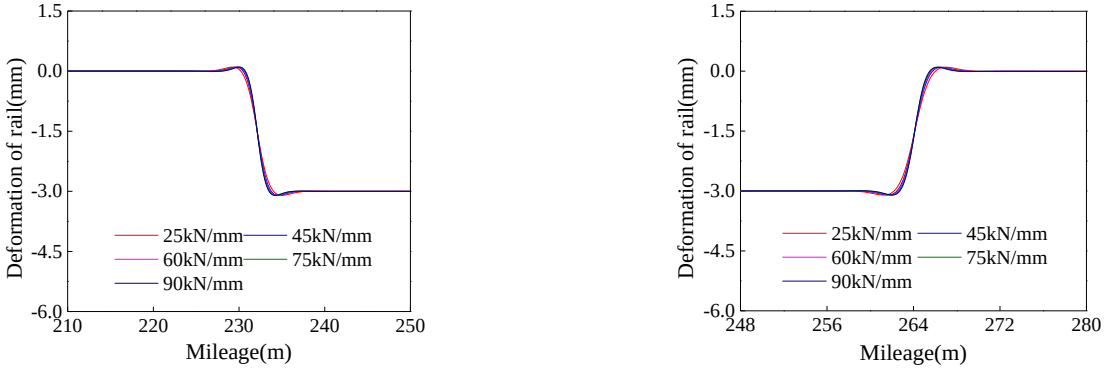

(a) The place of # 1 pier (b) The place of # 2 pier

Fig. 20 Effect of fastener stiffness on rail deformation for girder body vertical fault of 3 mm

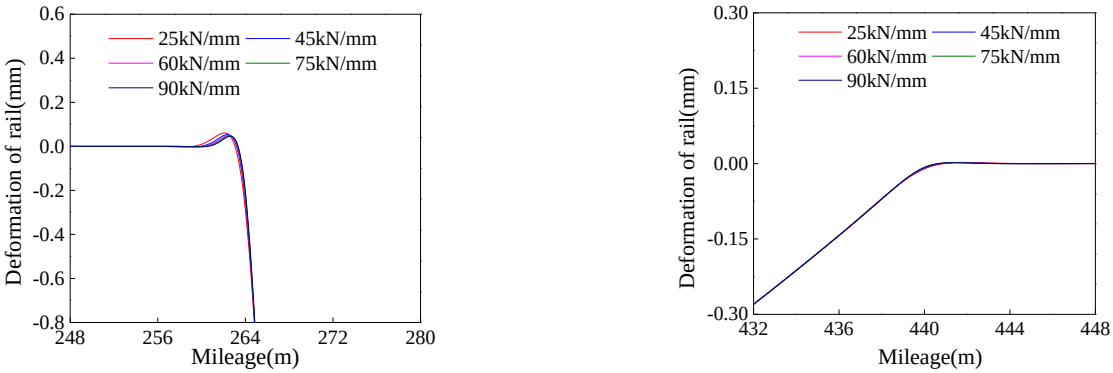

(a) The place of # 2 pier (b) The place of # 2 pier

Fig. 21 Effect of fastener stiffness on rail deformation for girder end vertical rotation of 1‰ rad

Table 5 Rail deformation region data for girder body fault and end rotation under different fasteners stiffness

Rail deformation	Fasteners' stiffness (kN/mm)									
	Girder body fault of 3 mm					Girder end rotation of 1‰ rad				
	25	45	60	75	90	25	45	60	75	90
L_r (m)	42.13	40.75	40.13	39.63	39.38	179.88	179.13	178.88	178.75	178.38
δ	1.316	1.273	1.254	1.238	1.230	1.022	1.018	1.016	1.016	1.013
M_{d-} (mm)	-3.101	-3.101	-3.100	-3.101	-3.101	-4.921	-4.908	-4.921	-4.908	-4.921
M_{d+} (mm)	0.101	0.101	0.101	0.101	0.101	0.702	0.702	0.702	0.702	0.702

Table 6 Computed results of rail deformation under different pier settlements

Continuous girder bridge span(m)	Rail deformation	Simplified girder bridge span(m)			
		2#pier settlement of 5 mm		3#pier settlement of 5 mm	
		24	32	24	32
32+48+32	L_r (m)	136.625	143.250	113.75	113.75
	δ	1.005	0.995	1.016	1.016
	M_{d-} (mm)	-4.908	-4.921	-5.033	-5.033
	M_{d+} (mm)	0.703	0.702	0.492	0.492
48+80+48	L_r (m)	200.125	206.75	176.000	176.000
	δ	1.001	0.994	1.000	1.000
	M_{d-} (mm)	-4.928	-4.936	-5.077	-5.077
	M_{d+} (mm)	0.809	0.808	0.439	0.439

induced by the piers' settlement gradually decreased. When fastener stiffness exceeded 45 kN/mm, the mapping region length and the mapping coefficient of the rails' deformation tended to be stable. While the amplitude of the upward deformation of the rails induced by the piers' settlement was not influenced in any significant manner by the fasteners' stiffness, the amplitude of the downward deformation of the rails induced by the piers' settlement increased with the increase of the fasteners' stiffness.

As can be seen in Table 5 and Figs. 20-21, under girder body vertical fault and girder end vertical rotation, with the increase of the vertical stiffness of fasteners, the mapping region length and mapping coefficient of the rails' deformation that was induced by girder body vertical fault gradually decreased, while the amplitude of the rails' deformation that was induced by girder body vertical fault was not influenced in any significant manner by fastener stiffness.

4.5 Influence of bridge span on rail deformations

To study the influence of bridges' span on rail deformations, the rail deformations of the HSRBST with different spans under three typical deformations of bridge structures were calculated; see calculation results in Tables 6-7. As can be seen in Tables 6-7, under the settlement of the 2# pier and girder end vertical fault, with the increase of simply supported girder span, the mapping region length of

Table 7 Computed results of rail deformation under girder body fault and girder end rotation

Continuous girder bridge span(m)	Rail deformation	Simplified girder bridge span(m)			
		Girder body fault of 3 mm		Girder end rotation of 1‰ rad	
		24	32	24	32
32+48+32	L_r (m)	32.125	40.125	114.875	114.875
	δ	1.339	1.254	1.025	1.025
	M_{d-} (mm)	-3.101	-3.101	-5.565	-5.565
	M_{d+} (mm)	0.101	0.101	2.501	2.501
48+80+48	L_r (m)	32.125	40.125	178.875	178.875
	δ	1.339	1.254	1.016	1.016
	M_{d-} (mm)	-3.101	-3.101	-8.408	-8.408
	M_{d+} (mm)	0.101	0.101	4.312	4.312

the rails' deformation increased, while the mapping coefficient decreased; under the settlement of the 2# pier, with the increase of simply supported girder span, the amplitude of the upward deformation of the rails decreased, while that of downward deformation increased; under girder end vertical fault, no obvious change was observed in either the amplitude of the upward deformation or that of the downward deformation. Under the 3# pier settlement and girder end rotation, with the increase of the continuous girder span, the mapping region length of the rail's deformation increased while the mapping coefficient decreased; under the settlement of the 3# pier, with the increase of the simply supported girder span, the amplitude of the upward deformation of the rails increased, while that of the downward deformation decreased. Under the girder end rotation, the amplitudes of the downward and upward deformation of the rails both increased. These results suggest that, with the increase of the bridges' span, the deformation curves became gentler, and the additional wavelength of the tracks' irregularity became longer.

5. Conclusions

Taking the interlayer interactions of HSRBST into account, the analytical method for calculating the mapping relationship between the vertical deformation of bridge structures and rail deformation was proposed. Then the analytical method and the finite element numerical method were used to calculate the rails' deformations under three typical deformations of bridge structures. Finally, the parametric analysis was carried out to analyze the factors influencing the rail deformation, and the following conclusions were drawn:

- The calculation results by the analytical method and the finite element numerical method were well agreed with each other under three typical deformations of bridge structures, which demonstrates the effectiveness of the analytical method proposed in this paper.
- Under three typical bridge structure deformations, the rail deformation first shows a trend of local upward and soon sinks when going in and out of the settlement region, which would increase the wheel-rail force when a train runs into the settlement region.
- The mapping coefficient between bridge structure deformation and rail deformation shows a nonlinear increase with increasing amplitude of bridge structure deformation, and a linear relationship was observed between the extreme values of the rail deformation and the amplitude of the bridge structures deformation.
- With increasing fastener stiffness, the mapping region length and mapping coefficient of rail deformation gradually decrease. With increasing bridge span, the deformation curve become gentler, and the wavelength of the additional track irregularity becomes longer.

Acknowledgments

The research described in this paper was financially supported by the Fundamental Research Funds for the Central Universities of Central South University (2018zzts189), the National Natural Science Foundations of China (51778630), and the Hunan Innovative Provincial Construction Project (2019RS3009).

References

Arisoy, B. and Erol, O. (2018), "Finite element model calibration of a steel railway bridge via ambient vibration test", *Steel Compos. Struct., Int. J.*, **27**(3), 327-335. https://doi.org/10.12989/scs.2018.27.3.327

Biondi, B., Muscolino, G. and Sofi, A. (2005), "A substructure approach for the dynamic analysis of train- track-bridge system", *Comput. Struct.*, **83**(28-30), 2271-2281. https://doi.org/10.1016/j.compstruc.2005.03.036

Cai, X., Liu W., Wang. P. and Ning. X. (2014), "Effect of land subsidence on regularity of double-block ballastless track", *Eng. Mech.*, **31**(9), 160-165. [In Chinese]

Chen, Z., Zhai, W., Cai, C. and Sun, Y. (2015), "Safety threshold of high-speed railway pier settlement based on train-track-bridge

dynamic interaction", *Sci. China: Technol. Sci.*, **58**(2), 202-210. https://doi.org/10.1007/s11431-014-5692-0

Chen, Z., Zhai, W. and Tian, G. (2018), "Study on the safe value of multi-pier settlement for simply supported girder bridges in high-speed railways", *Struct. Infrastruct. E*, **14**(3), 400-410. https://doi.org/10.1080/15732479.2017.1359189

Cheng, H., Li, H., Wang, D., Sun, Z., Li, G. and Jin, J. (2016), "Research on the influencing factors for residual displacements of RC bridge columns subjected to earthquake loading", *B Earthq. Eng.*, **14**(8), 2229-2257. https://doi.org/10.1007/s10518-016-9902-y

Feng, Y., Jiang, L., Zhou, W. and Han, J. (2019), "Lateral-torsional buckling of box beam with corrugated steel webs", *J. Central South Univ.*, **26**(7), 1946-1957. https://doi.org/10.1007/s11771-019-4122-0

Gou, H., Yang, L., Leng, D., Bao, Y. and Pu, Q. (2018a), "Effect of bridge lateral deformation on track geometry of high-speed railway", *Steel Compos. Struct., Int. J.*, **29**(2), 219-229. https://doi.org/10.12989/scs.2018.29.2.219

Gou, H., Zhou, W., Bao, Y., Li, X. and Pu, Q. (2018b), "Experimental study on dynamic effects of a long- span railway continuous beam bridge", *Appl. Sci.*, **8**(5), 669. https://doi.org/10.3390/app8050669

Gou, H., Yang, L., Mo, Z., Guo, W., Shi, X. and Bao, Y. (2019), "Effect of long-term bridge deformations on safe operation of high-speed railway and vibration of vehicle-bridge coupled system", *Int. J. Struct. Stab. Dyn.*, **19**(9), 1950111. https://doi.org/10.1142/S0219455419501116

He, X., Wu, T., Zou, Y., Chen, Y. F., Guo, H. and Yu, Z. (2017), "Recent developments of high-speed railway bridges in China", *Struct. Infrastruct. E*, **13**(12), 1584-1595. https://doi.org/10.1080/15732479.2017.1304429

He, C., Chen, Z. and He, Q. (2018), "Dynamic Behaviors of High Speed Train Running through Subgrade Bridge Transition Section", In: *ICRT 2017: Railway Development, Operations, and Maintenance*, Reston, VA, USA: American Society of Civil Engineers, pp. 197-206.

Jahangiri, M. and Zakeri, J. (2017), "Dynamic analysis of train-bridge system under one-way and two-way high-speed train passing", *Struct. Eng. Mech., Int. J.*, **64**(1), 33-44. https://doi.org/10.12989/sem.2017.64.1.033

Jiang, L., Feng, Y., Zhou, W. and He, B. (2018), "Analysis on natural vibration characteristics of steel- concrete composite truss beam", *Steel Compos. Struct., Int. J.*, **26**(1), 79-87. https://doi.org/10.12989/scs.2018.26.1.079

Jiang, L., Yu, J., Zhou, W., Feng, Y. and Chai, X. (2019a), "Analysis of flexural natural vibrations of thin-walled box beams using higher order beam theory", *Struct. Des. Tall Spec.*, **28**(14), 1-15. https://doi.org/10.1002/tal.1659

Jiang, L., Feng, Y., Zhou, W. and He, B. (2019b), "Vibration characteristic analysis of high-speed railway simply supported beam bridge-track structure system", *Steel Compos. Struct., Int. J.*, **31**(6), 591-600. https://doi.org/10.12989/scs.2019.31.6.591

Ju, S.H. (2013), "3D analysis of high-speed trains moving on bridges with foundation settlements", *Arch. Appl. Mech.*, **83**(2), 281-291. https://doi.org/10.1007/s00419-012-0653-1

Kang, X., Jiang, L., Bai, Y. and Caprani, C.C. (2017), "Seismic damage evaluation of high-speed railway bridge components under different intensities of earthquake excitations", *Eng. Struct.*, **152**, 116-128. https://doi.org/10.1016/j.engstruct.2017.08.057

Kun, C., Yang, Z. and Chouw, N. (2018), "Seismic response of skewed bridges including pounding effects", *Earthq. Struct., Int. J.*, **14**(5), 467-476. https://doi.org/10.12989/eas.2018.14.5.467

Lai, M., Hanzic, L. and Ho, J.C.M. (2018), "Fillers to improve passing ability of concrete", *Struct. Concrete*, **20**(1), 1-13. https://doi.org/10.1002/suco.201800047

Lee, J.S., Choi, S., Kim, S.S., Kim, Y.G., Kim, S.W. and Park, C. (2012), "Waveband analysis of track irregularities in high -speed railway from on board acceleration measurement", *J. Solid Mech. Mater. Eng.*, **6**(6), 750-759. https://doi.org/10.1299/jmmp.6.750

Li, X., Liang, L. and Wang, D. (2018), "Vibration and noise characteristics of an elevated box girder paved with different track structures", *J. Sound Vib.*, **425**, 21-40. https://doi.org/10.1016/j.jsv.2018.03.031

Ministry of Railways (2014), Code for design high speed railway; China Railway Press, Beijing, China.

Podworna, M. (2017), "Dynamic response of steel-concrete composite bridges loaded by high-speed train", *Struct. Eng. Mech., Int. J.*, **62**(2), 179-196. https://doi.org/10.12989/sem.2017.62.2.179

Qiao, H., Xia, H. and Du, X. (2018), "Dynamic analysis of an integrated train-bridge-foundation-soil system by the substructure method", *Int. J. Struct. Stab. Dyn.*, **18**(5), 1850069. https://doi.org/10.1142/S0219455418500694

Shi, R.X. (2013), "Influence of pier differential settlement on the track vertical profle irregularity", *Sichuan Architect.*, **1**, 94-99. [In Chinese]

Sun, L., Hayashikawa, T., He, X. and Xie, W. (2015), "Influential parameter analysis on vibration responses of rigid-frame viaducts induced by running high-speed trains", *Int. J. Steel Struct.*, **15**(4), 809-826. https://doi.org/10.1007/s13296-015-1204-8

Sun, L.M., Xie, W.P., He, X.W. and Hayashikawa, T. (2016), "Prediction and mitigation analysis of ground vibration caused by running high-speed trains on rigid-frame viaducts", *Earthq. Eng. Eng. Vib.*, **15**(1), 31-47. https://doi.org/10.1007/s11803-016-0303-7

Toydemir, B., Kocak, A., Sevim, B. and Zengin, B. (2017), "Ambient vibration testing and seismic performance of precast I beam bridges on a high speed railway line", *Steel Compos. Struct., Int. J.*, **23**(5), 557-570. https://doi.org/10.12989/scs.2017.23.5.557

Toyooka, A., Ikeda, M., Yanagawa, H., Kataoka, H., Iemura, H. and Murata, K. (2005), "Effects of track structure on seismic behavior of isolation system bridges", *Quarterly Report of RTRI*, **46**(4), 238-243. https://doi.org/10.2219/rtriqr.46.238

Wang, K., Liu, P., Zhai, W., Huang, C., Chen, Z. and Gao, J. (2015), "Wheel/rail dynamic interaction due to excitation of rail corrugation in high-speed railway", *Sci. China: Technol. Sci.*, **58**(2), 226-235. https://doi.org/10.1007/s11431-014-5633-y

Wei, Y., Xu, H. and Niu, B. (2010), "Laboratory test and numerical analysis on the mechanical behaviors of the slab track fastener due to the beam-ending deformation", *China Railway Sci.*, **31**(6), 43-49.

Wei, Y., Xu, H. and Niu, B. (2011), "Model test and numerical analysis of the influence of ballastless track bridge beam end deformation on fastener", *Railway Eng.*, **3**, 99-102. [In Chinese]

Xu, H. (2017), "Quantitative study on mapping relationship between bridge deformation and track geometry of high-speed railway", Southwest Jiaotong University, Chengdu, China.

Yau, J.D. (2009), "Response of a maglev vehicle moving on a series of guideways with differential settlement", *J. Sound Vib.*, **324**(3-5), 816-831. https://doi.org/10.1016/j.jsv.2009.02.031

Zhai, W., Zhao, C., Xia, H., Xie, Y., Li, G., Cai, C., Luo, Q. and Song, X. (2014), "Basic scientific issues on dynamic performance evolution of the high-speed railway infrastructure and its service safety", *Sci. China: Technol. Sci.*, **44**(7), 645-660. https://doi.org/10.1360/N092014-00192

Zhou, W. and Jiang, L. (2017), "Distortional buckling of cold-formed lipped channel columns subjected to axial compression", *Steel Compos. Struct., Int. J.*, **23**(3), 331-338.

https://doi.org/10.12989/scs.2017.23.3.331
Zhou, W.B., Jiang, L.Z. and Yu, Z.W. (2013), "Analysis of free vibration characteristic of steel-concrete composite box girder considering shear lag and slip", *J. Central South Univ.*, **20**(9), 2570-2577. https://doi.org/10.1007/s11771-013-1770-x

CC